Lossless Compression of Multidimensional Medical Images for Augmented Reality Applications

Bruno Carpentieri(✉) and Raffaele Pizzolante

Dipartimento di Informatica, Università degli Studi di Salerno,
84084 Fisciano, SA, Italy.
bc@dia.unisa.it, rpizzolante@unisa.it

Abstract. Medical digital imaging technologies produce daily a huge amount of data (data obtained by magnetic resonance, computed tomography and ultrasound examinations, functional resonance magnetic acquisitions, etc.), which is generally stored in ad-hoc repositories or it is transmitted to other entities, such as research centers, hospital structures, etc.. These data need efficient compression, in order to optimize memory space and transmission costs. In this work, we introduce an efficient lossless algorithm that can be used for the compression of volumetric multidimensional medical image sequences. This approach can be also used, in conjunction with Augmented Reality techniques, to save in a database or to transmit on a communication line the outcomes of surgical decisions or medical applications. We experimentally test our approach on a test set of 3-D computed tomography (CT), 3-D magnetic resonance (MR) images, and of 5-D functional Magnetic Resonance Images (fMRI). The achieved results outperform the other state-of-the-art approaches.

Keywords: Multidimensional medical images compression · Multidimensional medical images coding · Multidimensional data compression

1 Introduction

Digital medical images are widely used in a large range of medical applications, research tasks, medical related studies, etc.. The acquisition technologies are continuously evolving and are becoming always more sophisticated. On the other hand, the amount of memory space required for the storing and the time needed for the transmission is growing proportionally to the size of the images. The new expectations in medicine that are arising from the application of augmented reality techniques (see [6], [7]) will increase the need for memory space or the transmission time for medical data.

It is evident that data compression is essential, in order to minimize the implicit transmission costs involved. Since the compression layer is generally transparent or semi-transparent to the end-users, it is important to adopt models that can have high-level profiles (as for instance an *higher compression at lower speed* profile, or a *lower compression at higher speed* profile, etc.) or that are related to the hardware on which the compression process will be performed (as for instance *use resources as parsimoniously as possible*, etc.).

L.T. De Paolis and A. Mongelli (Eds.): AVR 2014, LNCS 8853, pp. 124–136, 2014.
DOI: 10.1007/978-3-319-13969-2_10

The design decisions related to the compression techniques need to consider which strategy (lossy or lossless) could be used in the delicate medical contexts. Today, lossy compression strategies are in a few case used, but lossless compression techniques are generally preferred, since they guarantee that the coded data, once decoded, are identical to the original data and this cheers and satisfies doctors.

In this paper, we consider lossless techniques that are based on the predictive model, described in [18]. We focus on multidimensional medical image sequences (such as 3-D computed tomography images, functional resonance magnetic images, etc.), which have considerable space memory requirements (many hundreds of megabytes/gigabytes per acquisition). These techniques can be also used coupled with Augmented Reality applications in medicine and tele-medicine.

State-of-the-art predictive-based schemes can be subdivided into two distinct and independent steps: modeling and coding [4]. The digital file is observed in a predefined order and modeling is aimed at gathering information in the form of a probabilistic model that is then used for coding. The modeling step can be carried out via a predictive structure, in which a value x^{t+1} is guessed for the next sample to be coded: x^{t+1}, based on a finite subset of the available past data. The prediction residual (or prediction error) can then be encoded conditionally on the context of x^{t+1}. The usual interpretation of prediction, which is the most important step of this scheme, is that it de-correlates the data samples, thus allowing the use of simple models (i.e. entropy coders) for the coding of prediction errors.

The purpose of this paper is to introduce a novel multidimensional, configurable, predictive structure that can be used for the compression of multidimensional medical images. The predictor we propose is scalable, adjustable, and adaptive. We present experimental evidences of its performance on multidimensional medical images: 3-D Computed Tomography (CT) images, 3-D Magnetic Resonance (MR) images and 5-D functional Magnetic Resonance Images (fMRI).

This paper is organized as follows: Section 2 focuses on the description of the proposed *N*–D predictive structure. In Section 3, we report the experimental results achieved on the different typologies of *N*–D data. Finally, we highlight our conclusions and outline future research directions (Section 4).

2 A Predictive Structure for Multidimensional Data

Formally, we can define a multidimensional (*N*-D) dataset as a collection of bi-dimensional components (such as images, data matrices, etc.) [11]. The dimensions of an *N*-D dataset ($N \geq 3$) can be described as $<M_1, M_2, \ldots, M_{N-2}, X, Y>$, where *X* and *Y* are respectively the width and the height of the bi-dimensional components and M_f is the size of the *f*-th dimension ($1 \leq f \leq N-2$). A specific bi-dimensional component can be univocally identified through a vector of *N*–2 elements: $[p_1, p_2, \ldots, p_{N-2}]$, where $p_i \in \{1,2,...,M_i\}$ [11].

By considering the formal definition of an *N*-D dataset, we can describe the dimensions of a three-dimensional (3-D) dataset as <*Z*, *X*, *Y*>. This means that the dataset is

composed of Z components (among the third dimension), where each component has respectively width X and height Y.

According to the above definitions of N-D data, let's suppose that the current sample has coordinates (m_1, m_2, …, m_{N-2}, x, y) (where $1 \le x \le X$, $1 \le y \le Y$ and $1 \le m_i \le M_i$, $\forall i \in \{1,2,\ldots, N-2\}$). Consequently, the vector $[m_1, m_2, \ldots, m_{N-2}]$ identifies the current component.

For each of the N–2 dimension, we define a *references set*, denoted as $R_i = \{r_1^i, r_2^i, \ldots, r_{t_i}^i\}$ (for the i-th dimension, with $1 \le i \le N-2$), where $r_j^i \in \{1,2,\ldots,M_i\} \cup \{-1,-2,\ldots,-M_i\}$, $t_i = |R_i|$, $1 \le j \le t_i$, and $\left|\bigcup_{i=1}^{N-2} R_i\right| > 0$.

Such references sets are univocally set up at the beginning of the algorithm and they are used in the prediction step.

In detail, a generic element $r_j^i \in R_i$ (where $1 \le i \le N-2$) will be used to denote a specific bi-dimensional component. In particular, we will use the following notation: if $r_j^i > 0$, then the denoted component is the one identified through the vector $[m_1, m_2, \ldots, m_{i-1}, r_j^i, m_{i+1}, \ldots, m_{N-2}]$, or, if $r_j^i < 0$, then the denoted component is the one identified through the vector $[m_1, m_2, \ldots, m_{i-1}, m_i - |r_j^i|, m_{i+1}, \ldots, m_{N-2}]$.

The proposed predictive model is based on the least squares optimization technique. In particular, the prediction is formed by using the current component and all the (valid) components of the *references sets*.

If we consider $N = 3$ and suppose that we have a 3-D medical image with dimensions: $M_1 = 48$ (Z dimension), $X = 256$ and $Y = 256$ (formally denoted as <48, 256, 256>). For example, we can set up the references set for the M_1 dimension (Z dimension) as $R_1 = \{-1, -2\}$ and we suppose that the current sample has (23, 45, 67) as coordinates ($m_1 = 23$, $x = 45$ and $y = 67$). Therefore, in this example, the prediction is formed by using the neighboring samples of the current sample in the current component, identified by the vector *[23]*, and in the components identified by the vectors *[22]* (*[23 – |–1|]*) and *[21]* (*[23 – |–2|]*). In detail, these latter vectors, *[22]* and *[21]*, are obtained by considering respectively the element –1 and the element –2 of R_1.

Let E denotes a 2-D enumeration, which has as objective the relative indexing of the samples in a bi-dimensional context, with respect to a specific reference sample. The fundamental requisites that the enumeration E needs to satisfy are that the specified reference sample has 0 as index and that any two samples (with different coordinates) do not have the same index.

Let $x_j^{(e)}(r_s^j)$ (where $r_s^j \in R_j$) denotes the e-th sample in the bi-dimensional context according to the enumeration E, with respect to the sample with coordinates (m_1, m_2, …, m_{j-1}, r_s^j, m_{j+1}, …, m_{N-2}, x, y) when $r_s^j > 0$, or (m_1, m_2, …, m_{j-1}, $m_j - |r_s^j|$, m_{j+1}, …, m_{N-2}, x, y) when $r_s^j < 0$.

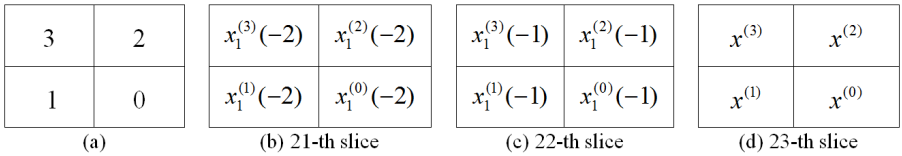

(a) (b) 21-th slice (c) 22-th slice (d) 23-th slice

Fig. 1. (a) An example of an enumeration; Examples of the bi-dimensional prediction contexts for: (b) the 21-th, (c) the 22-th and (d) the 23-th slice

Finally, let $x^{(e)}$ denotes the *e*-th sample in the current component, according to the enumeration *E*, with respect to the current sample. Notice that $x^{(0)}$ denotes precisely the current sample.

By taking into consideration the previous example, we consider, for instance, the enumeration *E* graphically defined in Figure 1(a). Figures 1(b), 1(c) and 1(d) show the bi-dimensional prediction contexts, obtained by using the enumeration of Figure 1(a), respectively for the 21-th, 22-th and 23-th slices (formally identified respectively through the vectors *[21]*, *[22]* and *[23]*) and highlight how the samples are addressed according to our notations.

The *T*-order prediction (where $T=\sum_{i=1}^{N-2} t_i = \sum_{i=1}^{N-2} |R_i|$) of the current sample $x^{(0)}$ is obtained through the equation (1).

$$\hat{x}^{(0)} = \sum_{i=1}^{N-2} \sum_{j=1}^{t_i} \alpha_i^j \cdot x_i^{(0)}(r_j^i) \,. \tag{1}$$

The coefficients $\alpha_0 = [\alpha_1^1,...,\alpha_1^{t_1},...,\alpha_i^1,...,\alpha_i^{t_i},...,\alpha_{N-2}^1,...,\alpha_{N-2}^{t_{N-2}}]^t$ are chosen to minimize the energy of the prediction error:

$$P = \sum_{i=1}^{H} \left(x^{(i)} - \hat{x}^{(i)}\right)^2 \,. \tag{2}$$

In detail, *H* indicates the number of samples used, for the current and for each one of the components specified in the references sets. Thus, $H \cdot (T + 1) + T$ samples are used for the prediction.

The coefficients α_0 are obtained by using the optimal linear prediction method, as in [17]. In detail, we can rewrite the equation (2) in the form $P = (\boldsymbol{C}\alpha - \boldsymbol{X})^t \cdot (\boldsymbol{C}\alpha - \boldsymbol{X})$, by using matrix notation, where:

$\boldsymbol{C}=$

$$\begin{bmatrix} x_1^{(1)}(r_1^1) & \dots & x_1^{(1)}(r_{t_1}^1) & \cdots & x_i^{(1)}(r_1^i) & \dots & x_i^{(1)}(r_{t_i}^i) & \cdots & x_{N-2}^{(1)}(r_1^{N-2}) & \dots & x_{N-2}^{(1)}(r_{t_{N-2}}^{N-2}) \\ \vdots & \ddots & \vdots & & \vdots & \ddots & \vdots & & \vdots & \ddots & \vdots \\ x_1^{(H)}(r_1^1) & \dots & x_1^{(H)}(r_{t_1}^1) & \cdots & x_i^{(H)}(r_1^i) & \dots & x_i^{(H)}(r_{t_i}^i) & \cdots & x_{N-2}^{(H)}(r_1^{N-2}) & \dots & x_{N-2}^{(H)}(r_{t_{N-2}}^{N-2}) \end{bmatrix}$$

and $\boldsymbol{X} = [\, x^{(1)} \quad \cdots \quad x^{(H)} \,]^t$.

The linear system of the equation (3) is obtained, as in [17], by taking the derivate of the equation (2), in matrix notation, with respect to α , and by setting it to zero.

$$(\boldsymbol{C}^t\boldsymbol{C})\ \alpha_0 = (\boldsymbol{C}^t\boldsymbol{X}). \tag{3}$$

Thus, by computing the coefficients α_0, which solve the linear system (3), it is possible to determinate the prediction of the current sample, $\hat{x}^{(0)}$, by using the equation (1).

In particular, the prediction error is computed by means of the equation (4). This latter can then be sent to an entropy encoder.

$$e = \left\lfloor x^{(0)} - \hat{x}^{(0)} \right\rfloor. \tag{4}$$

The proposed predictive model is easily scalable through an adequate configuration of the references sets. By selecting the wideness of the multidimensional prediction context, which depends on *H*, it is possible to configure the predictive model in order to prefer the parsimonious use of the computational resources, so to make the model suitable for low-complexity applications, or it is possible to reward the accurateness of the prediction. It is important to note, that if we use only past information there is no need to send any side information to the decompression algorithm during the prediction step.

If the linear system of the equation (3) has no solutions or if it has infinitely, many solutions [9], our approach cannot perform the prediction. We called these scenarios *exceptions* and the exceptions can be managed through another predictive model (for example DPCM, Median Predictor, etc.).

3 Experimental Results

We have tested our predictive model by implementing a predictive-based compression scheme, and then we have experimented this algorithm on different types of *N*-D data: 3-D computed tomography and 3-D magnetic resonance images (Sec. 3.1), and 5-D fMRI medical images (Sec. 3.2).

The algorithm takes as input the *N*-D images and predicts the current sample, by using the previously coded samples. In this way, it is possible to have a consistent prediction for both compression and decompression algorithm.

After the prediction step, the prediction error is obtained as the difference between the current sample and its prediction. Finally, the prediction error can be encoded by using an entropy or a statistical coder.

In our experiments, we have used as error encoder the PAQ8 algorithm, which is a state-of-the-art lossless compression algorithm [10]. In particular, the PAQ8 method belongs to the PAQ family, which is an Open Source compression family. As discussed in [10], such family of encoders is strictly related to the well-established *Prediction by Partial Matching* scheme (PPM), which is described in [18].

		32	26	24	27			
	29	20	16	14	17	21	30	
31	19	11	8	6	9	12	22	
25	15	7	3	2	4	10	18	28
23	13	5	1	**(0)**				

Fig. 2. Example of the resulting enumeration E of the first 32 samples, based on the function defined in (5)

From the design point of view, some architectural aspects could vary depending on the particular version of PAQ8. In detail, we used the *paq8l* version (released by Matt Mahoney) that uses 552 predictive structures. Such predictive structures are modeled in a single prediction through a *Model Mixer*. Once the prediction is computed, the result of such step is passed to an *Adaptive Probability Map* (APM). After this, the obtained prediction error is used by the arithmetic encoder scheme [18]. The main objective of an APM is to reduce the prediction error of 1% [10]. Furthermore, in order to improve the accuracy, the values composing an APM are adjusted according to the prediction error, after the encoding of each bit of the input data [10]. Generally, all the versions of the PAQ8 algorithm achieve a high degree of compression performances. On the other hand, the complexity is over the average of other lossless approaches.

In detail, the implementation of the proposed method uses the 2-D Linearized Median Predictor (2D-LMP) [15], for all the components which have no component references (for instance, the first slice of a 3-D medical image), and our N-D predictive structure, for all the other components.

As enumeration E, similarly to [17], we have used the one that is based on the distance function d, defined as:

$$d((m_1,...,m_{N-2},u,v),(m_1,...,m_{N-2},w,z)) = \sqrt{(u-w)^2+(v-z)^2}\ .$$

Figure 2 shows an example of the resulting enumeration E for the first 32 samples, by using as reference sample the sample that has 0 as index (highlighted in parenthesis in Fig. 2).

In order to improve the readability, we use the mnemonic name of the dimension instead of its index for the references sets. For example, R_Z indicates the reference set for the Z dimension.

3.1 3-D Medical Images

We have performed experiments on the test set described in Table 1, which is composed by four 3-D CT images and four 3-D MR images. It is important to outline that each slice has 256 columns, 256 lines and each sample is stored by using 8 bits.

Table 1. Description of the used test set

3-D Computed Tomography Images		
***Description* – Age – Gender**	**Image Name**	**Number of slices**
Tripod fracture – 16 – M	CT_skull	192
Healing scaphoid dissection – 20 – M	CT_wrist	176
Internal carotid dissection – 41 – F	CT_carotid	64
Apert's syndrome – 2 – M	CT_Aperts	96
3-D Magnetic Resonance Images		
***Description* – Age – Gender**	**Image Name**	**Number of slices**
Normal – 38 – F	MR_liver_t1	48
Normal – 38 – F	MR_liver_t2e1	48
Left exophthalmos – 42 – M	MR_sag_head	48
Congenital heart disease – 1 – M	MR_ped_chest	64

In the next two sub-sections, we report the experimental results achieved respectively for the 3-D CT and 3-D MR images.

In both cases, as in [12], we have mapped the prediction error before coding through the PAQ8 scheme. Furthermore, we have managed the exceptions with the 3-D Differences-based Linearized Median Predictor (3D-DLMP) [15].

3-D Computed Tomography Images. Computed Tomography (also known as TC, CT, TAC and CAT) uses X-rays to obtain many radiological images. During this process is used a computer, in order to produce different cross-sectional views. It is also possible to obtain three-dimensional views of internal organs of the body.

One of the most common medical application is generally related to identify normal or abnormal structures of the human body. Generally, an X-ray scanner generates many different X-ray images at various angles around the body. All of these images are processed through the dedicated computer, which outputs cross-sectional images, generally referred as slices.

Thus, each slice is a graphical representation of a cross-section of the part of the human body that is undergoing analysis.

We have experimented our approach on the four 3-D CT images of the test set. In particular, in Table 2 we report the experimental results we have achieved, in terms of *bits-per-sample* (BPS), and we compare our results with other state-of-the-art techniques (first column), and we do this for each one of the four 3-D CT images (from the second to the fifth columns). Finally, the sixth column reports the average results for each method. It is important to remark that we have tested our approach by using different configurations for the H parameter and the references sets.

Figure 3 summarizes the results of Table 2. On the Y-axis we have the average bits-per-sample obtained on the 3-D CT images and on the X-axis we have the methods we are comparing. The configuration shown for our approach is: H=8, R_Z={-1, -2}.

As it is clear in Figure 3, our approach outperforms, all the other state-of-the-art techniques.

Table 2. Comparison of different compression methods on the CT data set. The results are reported in *bits-per-sample* (BPS).

	Methods / Images	CT_skull	CT_wrist	CT_carotid	CT_Aperts	*Average*
Proposed	H=32, R_Z={-1, -2, -3}	1.4836	0.8979	1.2783	0.7283	*1.0970*
	H=16, R_Z={-1, -2, -3}	1.5309	0.9290	1.2976	0.7350	*1.1231*
	H=8, R_Z={-1, -2, -3}	1.6258	1.0042	1.3421	0.7587	*1.1827*
	H=32, R_Z={-1, -2}	1.5393	0.9527	1.3363	0.7265	*1.1387*
	H=16, R_Z={-1, -2}	1.5688	0.9737	1.3448	0.7271	*1.1536*
	H=8, R_Z={-1, -2}	1.6196	1.0110	1.3496	0.7349	*1.1788*
	3D-ESCOT [19]	1.8350	1.0570	1.3470	0.8580	*1.2743*
	MILC [15]	2.0306	1.0666	1.3584	0.8190	*1.3187*
	AT-SPIHT [5]	1.9180	1.1150	1.4790	0.9090	*1.3553*
	3D-CB-EZW [3]	2.0095	1.1393	1.3930	0.8923	*1.3585*
	DPCM+PPMd [1]	2.1190	1.0290	1.4710	0.8670	*1.3715*
	3D-SPIHT [19]	1.9750	1.1720	1.4340	0.9980	*1.3948*
	3D-EZW [3]	2.2251	1.2828	1.5069	1.0024	*1.5043*
	JPEG-LS [4]	2.8460	1.6531	1.7388	1.0637	*1.8254*

In details, only for "*CT_carotid*", by using H=8 and R_Z={-1, -2}, our approach achieves a slightly worse results with respect to 3-D ESCOT, which is he most performing competitor.

3-D Magnetic Resonance Images. Magnetic Resonance Imaging (MRI) techniques are widely used for the investigation of the anatomy and the function of the body. In particular, the MRI scanners are able to produce three-dimensional images of the body, by using magnetic fields.

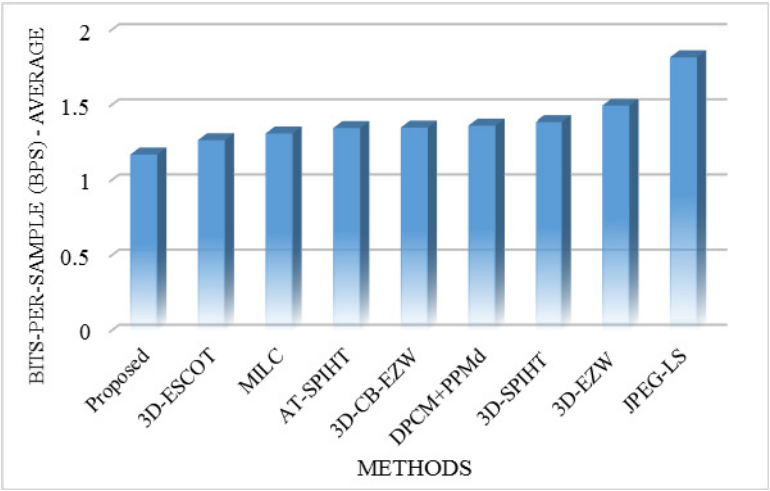

Fig. 3. Graphical comparison of different compression methods on the CT data

Table 3. Comparison of different compression methods on the MR data set. The results are reported in *bits-per-sample* (BPS).

	Methods / Images	MR_liver_t1	MR_liver_t2e1	MR_sag_head	MR_ped_chest	*Average*
Proposed	H=32, R_Z={-1, -2, -3}	1.8511	1.2539	1.4890	1.2920	*1.4715*
	H=16, R_Z={-1, -2, -3}	1.8850	1.2783	1.5311	1.3498	*1.5111*
	H=8, R_Z={-1, -2, -3}	1.9894	1.3360	1.6020	1.4669	*1.5986*
	H=32, R_Z={-1, -2}	1.8996	1.3101	1.5477	1.3740	*1.5329*
	H=16, R_Z={-1, -2}	1.9089	1.3232	1.5737	1.4053	*1.5528*
	H=8, R_Z={-1, -2}	1.9471	1.3482	1.6094	1.4694	*1.5935*
	3D-ESCOT	2.0760	1.5100	1.9370	1.6180	*1.7853*
	MILC	2.1968	1.7590	2.0975	1.6556	*1.9272*
	3D-SPIHT	2.2480	1.6700	2.0710	1.7420	*1.9328*
	3D-CB-EZW	2.2076	1.6591	2.2846	1.8705	*2.0055*
	DPCM+PPMd	2.3900	2.0250	2.1270	1.6890	*2.0578*
	3D-EZW	2.3743	1.8085	2.3883	2.0499	*2.1553*
	JPEG-LS	3.1582	2.3692	2.5567	2.9282	*2.7531*

There are many medical and medical-related fields, in which MRI techniques are involved. In particular, their most common use is related to medical diagnosis and treatments.

Table 3 reports the experimental results, in terms of *bits-per-sample* (BPS), achieved by our approach on the four 3-D MR images of our test set, by using different configurations for both the *H* parameter and the references set. We compared these results with the other state-of-the-art techniques.

Figure 4 summarizes the results of Table 3 and demonstrates that our approach outperforms all the other state-of the-art methods.

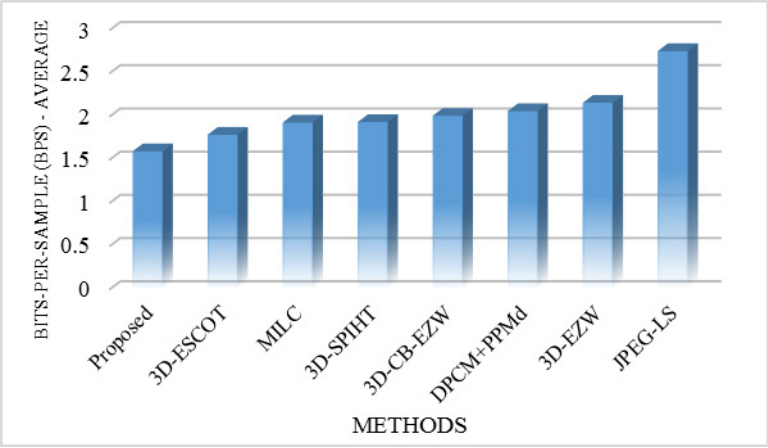

Fig. 4. Graphical comparison of different compression methods on the MR data

3.2 5-D Functional Magnetic Resonance Images

Functional Magnetic Resonance Imaging (functional-MRI or fMRI) is a technology used in different medical and research fields. fMRI permits, for example, the measurement of the brain activity through the measure of the changes of the cerebral blood flow [8], which is strongly coupled with the neuronal activation. An fMRI dataset consists in a collection of 3-D data volumes (*T* dimension). Each of them can be viewed as a collection (on the *Z* dimension) of bi-dimensional images (*X* and *Y* dimensions). Analyzing these data it is possible to determinate the regions of the brain that are activated by a particular task. Generally, multiple trials of experiments are performed (*R* dimension) to improve the accuracy of the examination. Therefore, these are 5-D data.

We have tested our approach on a test set, named *"Stop-signal task with unconditional and conditional stopping"* [2], that is currently available from the OpenfMRI project site [14]. The test set is composed of thirty 5-D fMRI images and has the following organization: there are two 5-D fMRI images (*task001* and *task002*) for each one of the fifteen studied subjects. *task001* and *task002* have respectively the following dimensions *R*=3, *T*=182, *Z*=30, *X*=64, and *Y*=64 and *R*=3, *T*=176, *Z*=30, *X*=64 and

Y=64; except for few exceptions where *R* can be different (*i.e.* *R*=1 or *R*=2). Each sample is stored by using 16 bits. Table 4 reports the experimental results we have achieved in terms of *bits-per-sample* (BPS). We have tested our approach with different parameters for the references sets. *H* is equal to 32. The exceptions are managed by DPCM [1] on the *Z* dimension.

Table 4. The 5-D fMRI data test set results are reported in *bits-per-sample* (BPS)

Dataset/ Proposed (Parameters)	3-D (Z)		3-D (T)		4-D		5-D	
	R_Z={ -1 }		R_T={ -1 }		R_Z={ -1 } R_T={ -1 }		R_R={ -1 } R_T={ -1 }, R_Z={ -1 }	
	task001	task002	task001	task002	task001	task002	task001	task002
sub001	6.5155	6.5095	5.3550	5.3513	5.3459	5.3421	5.3104	5.2983
sub002	6.8036	6.7873	5.4296	5.4266	5.4277	5.4238	5.3687	5.3844
sub003	6.5791	6.5641	5.3857	5.3469	5.3761	5.3385	5.3338	5.3032
sub004	7.0789	7.0860	5.7552	5.7686	5.7523	5.7662	5.7064	5.7046
sub005	6.6956	6.6908	5.4645	5.4463	5.4574	5.4395	5.4384	5.3989
sub006	6.6714	6.6638	5.5046	5.5081	5.4928	5.4960	5.4601	5.4779
sub007	6.9816	6.9473	5.4636	5.4745	5.4642	5.4761	5.4315	5.4434
sub008	6.6152	6.6119	5.3296	5.3266	5.3239	5.3211	5.3239	5.2853
sub009	6.8820	*N.P.*[1]	5.4410	*N.P.*[1]	5.4437	*N.P.*[1]	5.4265	*N.P.*[1]
sub010	6.7509	6.7450	5.4445	5.4342	5.4385	5.4281	5.4171	5.4176
sub011	6.6081	6.5977	5.3399	5.3252	5.3312	5.3162	5.3158	5.3184
sub012	6.8235	6.8583	5.4756	5.5145	5.4763	5.5150	5.4440	5.4990
sub013	6.6585	6.6492	5.4835	5.4825	5.4722	5.4705	5.4303	5.4403
sub014	6.7979	6.8154	5.5139	5.5319	5.5070	5.5259	5.4711	5.5150
sub015	6.6019	6.5900	5.4626	5.4543	5.4505	5.4426	5.4234	5.4248

[1]*N.P.*: Such data is not present into the test set.

The experimental results show that our approach achieves better results when our predictive model uses all the five dimensions: *X*, *Y*, *Z*, *T* and *R* (fifth column). When the predictive model uses *X*, *Y*, *Z* and *T* (fourth column), the results are generally slightly better with respect to the results achieved by using *X*, *Y*, *T* (third column) and they are significantly better with respect to when we have used *X*, *Y*, *Z* (second column). For such test set, to the best of our knowledge, there are no published results for other compression methods.

4 Conclusions and Future Work

In this paper, we have proposed an *N*-D predictive model that can be used for efficient lossless compression of multidimensional medical image. We have experimentally tested our method on 3-D computed tomography images, 3-D magnetic resonance images and 5-D functional Magnetic Resonance Imaging (fMRI) data.

Future work will include further testing of our approach, both for lossy and lossless compression, on other multidimensional data (eg. 4-D medical ultrasound images, etc.). We will also focus on the execution performances. In particular, we will outline a parallel implementation of our proposed approach, that can be executed on heterogeneous devices, such as Graphics Processing Units (GPUs), Central Processing Units (CPUs), Field Programmable Gate Arrays (FPGAs), etc.. We will finally design a multidimensional component or volume reordering algorithm, that will improve the compression performances [13, 16] without altering the complexity of the decoder.

References

1. Ait-Aoudia, S., Benhamida, F., Yousfi, M.: Lossless Compression of Volumetric Medical Data. In: Levi, A., Savaş, E., Yenigün, H., Balcısoy, S., Saygın, Y. (eds.) ISCIS 2006. LNCS, vol. 4263, pp. 563–571. Springer, Heidelberg (2006)
2. Aron, A.R., Behrens, T.E., Smith, S., Frank, M.J., Poldrack, R.A.: Triangulating a Cognitive Control Network Using Diffusion-Weighted Magnetic Resonance Imaging (MRI) and Functional MRI. The Journal of Neuroscience **27**(14), 3743–3752 (2007)
3. Bilgin, A., Zweig, G., Marcellin, M.W.: Three-Dimensional Image Compression with Integer Wavelet. Applied Optics **39**(11), 1799–1814 (2000)
4. Carpentieri, B., Weinberger, M., Seroussi, G.: Lossless Compression of Continuous Tone Images. Proceeding of IEEE **88**(11), 1797–1809 (2000)
5. Cho, S., Kim, D., Pearlman, W.A.: Lossless Compression of Volumetric Medical Images with Improved Three-Dimensional SPIHT Algorithm. Journal of Digital Imaging **17**(1), 57–63 (2004)
6. De Paolis, L.T., Pulimeno, M., Aloisio, G.: Advanced Visualization and Interaction Systems for Surgical Pre-operative Planning. CIT 18(4) (2010)
7. De Paolis, L.T., Ricciardi, F., Dragoni, A.F., Aloisio, G.: An Augmented Reality Application for the Radio Frequency Ablation of the Liver Tumors. In: Murgante, B., Gervasi, O., Iglesias, A., Taniar, D., Apduhan, B.O. (eds.) ICCSA 2011, Part IV. LNCS, vol. 6785, pp. 572–581. Springer, Heidelberg (2011)
8. fMRI Wikipedia English Page. http://en.wikipedia.org/wiki/Fmri (accessed on July 2014)

9. Golub, G.H., Van Loan, C.F.: Matrix Computations, 3rd ed. Baltimore. MD: The Johns Hopkins Univ. Press (1996)
10. Knoll, B., De Freitas, N.: A Machine Learning Perspective on Predictive Coding with PAQ8. Data Compression Conference (DCC) **24**(8), 377–386 (2012)
11. Lalgudi, H.G., Bilgin, A., Marcellin, M.W., Nadar, M.S.: Compression of Multidimensional Images Using JPEG2000. IEEE Signal Processing Letters **15**, 393–396 (2008)
12. Motta, G., Storer, J.A., Carpentieri, B.: Lossless Image Coding via Adaptive Linear Prediction and Classification. Proceedings of the IEEE **88**(11), 1790–1796 (2000)
13. Motta, G., Rizzo, F., Storer, J.A.: Hyperspectral Data Compression. Springer Science, Berlin (2006)
14. OpenfMRI Site. https://openfmri.org (accessed on July 2014)
15. Pizzolante, R., Carpentieri, B.: Lossless, low-complexity, compression of three-dimensional volumetric medical images via linear prediction. Digital Signal Processing (DSP), 1–6 (July 1-3, 2013)
16. Pizzolante, R., Carpentieri, B.: Visualization, Band Ordering and Compression of Hyperspectral Images. Algorithms **5**, 76–97 (2012)
17. Rizzo, F., Carpentieri, B., Motta, G., Storer, J.A.: Low-complexity lossless compression of hyperspectral imagery via linear prediction. IEEE Signal Processing Letters **12**(2), 138–141 (2005)
18. Salomon, D., Motta, G.: Handbook of Data Compression, 5 edn. Springer (2010) ISBN: 978-1-84882-902-2
19. Xiong, Z., Wu, X., Cheng, S., Jianping, H.: Lossy-to-lossless compression of medical volumetric data using three-dimensional integer wavelet transforms. IEEE Trans. on Medical Imaging **22**(3), 459–470 (2003)